ARTICLES
PUBLISHED ONLINE: 29 FEBRUARY 2016 | DOI: 10.1038/NCHEM.2450
nature chemistry

Carbon dioxide transport in molten calcium carbonate occurs through an oxo-Grotthuss mechanism via a pyrocarbonate anion

Dario Corradini[1,2,3], François-Xavier Coudert[4]* and Rodolphe Vuilleumier[1,2,3]*

The reactivity, speciation and solvation structure of CO_2 in carbonate melts are relevant for both the fate of carbon in deep geological formations and for its electroreduction to CO (to be used as fuel) when solvated in a molten carbonate electrolyte. In particular, the high solubility of CO_2 in carbonate melts has been tentatively attributed to the formation of the pyrocarbonate anion, $C_2O_5^{2-}$. Here we study, by first-principles molecular dynamics simulations, the behaviour of CO_2 in molten calcium carbonate. We find that pyrocarbonate forms spontaneously and the identity of the CO_2 molecule is quickly lost through O^{2-} exchange. The transport of CO_2 in this molten carbonate thus occurs in a fashion similar to the Grotthuss mechanism in water, and is three times faster than molecular diffusion. This shows that Grotthuss-like transport is more general than previously thought.

Carbonatite melts, mostly composed of XCO_3 (X = Li_2, Na_2, K_2, Mg, Ca), have recently received a great deal of attention[1,2]. It has been proposed that they are the most conductive phase in Earth's upper mantle, and they may determine the mobility and long-term storage of deep carbon, especially if found in the lower mantle[3–5]. Analysis of conductivity data has led to estimations of a 0.035–0.35% content of carbonatites by volume in the asthenosphere, in line with the estimated CO_2 content in magmas[1]. CO_2 from geological formations is mostly released into the atmosphere during volcanic activity, although the efficiency of CO_2 degassing remains poorly known[6]. Despite the importance of CO_2 species for the deep carbon cycle[7], the reactivity, speciation and solvation structure of CO_2 in carbonatite melts have so far remained unexplored.

New technologies capable of reducing the carbon footprint are greatly in demand, in particular to limit the impact of CO_2 on the environment. One of the strategies considered in the context of carbon capture and valorization consists of its dissolution in a molten carbonate medium and its subsequent electroreduction to CO[8–10]. The interaction between CO_2 and carbonates is thus relevant for environmental science and engineering beyond geochemistry.

In the context of the electrochemical reduction of CO_2, it has been observed that the solubility of CO_2 in the carbonate electrolyte is higher than would be expected simply from the expression $x^l_{CO_2} = k_H P_{CO_2}$, where $x^l_{CO_2}$ is the concentration of CO_2 in the liquid, k_H is Henry's constant and P_{CO_2} is the CO_2 partial pressure. To explain this increased solubility, a reaction of CO_2 with the carbonate anion has been hypothesized:

$$CO_2 + CO_3^{2-} \rightleftharpoons C_2O_5^{2-} \quad (1)$$

with the product of the reaction being called pyrocarbonate (or dicarbonate)[8–10]. Taking K_{pyro} as the equilibrium constant of this chemical reaction, one can then define an apparent Henry's constant $k_H^{app} = (1 + K_{pyro})k_H$. Thus it is possible that the CO_2/pyrocarbonate equilibrium controls the solubility of CO_2 in molten carbonates. Although this equilibrium can contribute to a larger CO_2 uptake in molten carbonates, it is not clear whether this is favourable for electrochemical processes, as the CO_2 involved in pyrocarbonate may not be readily accessible depending on the rate of interconversion. It is thus crucial to obtain a better understanding of CO_2 solvation in molten carbonates at the molecular level.

A limited number of previous studies have provided some support to the possibility of the formation of pyrocarbonate. The existence of a CO_2/pyrocarbonate equilibrium was first hypothesized by Claes and colleagues on the basis of experiments performed on the Li–Na–K carbonate eutectic mixture[11]. This has also been supported by gas-phase calculations[12]. It was later shown, using density functional theory (DFT) calculations, that in the gas phase $C_2O_5^{2-}$ and larger oligomers $C_nO_{2n+1}^{2-}$ are structurally stable, with their energetics being strongly dependent on the counterion[13]. Polymeric phases of CO_2 have also been predicted by DFT[14]. Zhang and co-workers have provided evidence of the presence of pyrocarbonate in Raman spectroscopy experiments, performed by exposing molten carbonate mixtures to a CO_2 atmosphere[15]. Finally, pyrocarbonate has also been invoked to explain NMR spectra in aqueous carbonate solutions[16].

Recently, two first-principles molecular dynamics (FPMD) studies have addressed the properties of molten carbonates[17] and of CO_2 in silicate melts[18]. The first study provided information relevant for the study of liquid $CaCO_3$, until then poorly explored in experiments, such as its liquid structure, density, atomic vibration motions, diffusion coefficients and electrical conductivity. In the second, the speciation of CO_2 in basaltic and kimberlitic melts in the CaO–MgO–Al_2O_3–SiO_2 system was investigated. Importantly, the formation of $C_2O_5^{2-}$ has been observed in the basaltic melt, accounting for ~3.7% of the C content in the system. Pyrocarbonate has been found to be a transient species with a very short mean lifetime of 175 fs, too short to assess its solvation structure and formation/dissociation dynamics.

In this study, we focus on CO_2 in molten $CaCO_3$, with the aim of characterizing the formation/dissociation of the pyrocarbonate and the solvation structure of CO_2 and pyrocarbonate in the melt. Using

[1]Department of Chemistry, École Normale Supérieure - PSL Research University, 24 rue Lhomond, 75005 Paris, France. [2]Sorbonne Universités, UPMC Univ. Paris 06, PASTEUR, 75005 Paris, France. [3]CNRS, UMR 8640 PASTEUR, 75005 Paris, France. [4]PSL Research University, Chimie ParisTech – CNRS, Institut de Recherche de Chimie Paris, 75005 Paris, France. *e-mail: fx.coudert@chimie-paristech.fr; rodolphe.vuilleumier@ens.fr

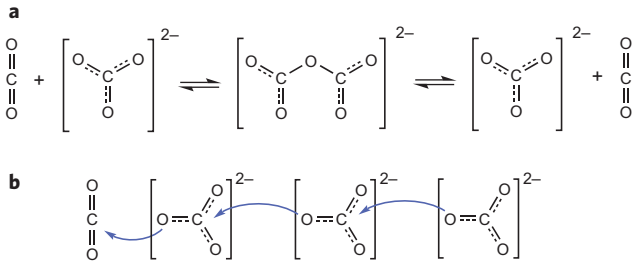

Figure 1 | Oxo-Grotthus mechanism via a pyrocarbonate anion. **a**, Formation of the pyrocarbonate ion $C_2O_5^{2-}$ from the reaction of CO_2 with carbonate anion CO_3^{2-}. **b**, A cascading mechanism, with rapid sequence of pyrocarbonate formation and dissociation events.

FPMD simulations, we confirm the presence of pyrocarbonate, which exists in rapid exchange with separate CO_2 and carbonate. The pyrocarbonate ion lives longer in $CaCO_3$ than in the basaltic melt reported in ref. 18, allowing us to study the details of its solvation structure, beyond its geometry. In addition, we find that the transport of CO_2 in molten carbonate occurs in a manner similar to the Grotthuss mechanism for proton transport in water, via independent events of formation and dissociation of the pyrocarbonate molecule.

Results and discussion

Formation of pyrocarbonate anion. Using FPMD simulations, we studied the behaviour of one CO_2 molecule in the $CaCO_3$ solvent. From analysis of the simulation trajectory, we observed the spontaneous formation of the pyrocarbonate ion $C_2O_5^{2-}$ out of the reaction of CO_2 with the carbonate anion CO_3^{2-}, as shown in Fig. 1a. There is a rapid exchange between the species, with multiple instances of formation and dissociation of the pyrocarbonate ion (79 events each in the simulation time span of 65 ps). To define the molecular species from the FPMD simulation trajectory, it is necessary to use a distance criterion, usually determined by looking at the minimum of the pair radial distribution functions (RDFs). We used a 'hysteresis' criterion with minimal/maximal C–O* distances, where O* is the central pyrocarbonate ion linking the two C atoms, C–O*–C (the other oxygen atoms in pyrocarbonate are simply termed O in the following; see Methods for further details). The minimal/maximal distances considered were 1.7 Å/1.95 Å, because within this span the C–O pair RDF is practically zero for molten carbonates.

With the abovementioned criteria we observed the presence of pyrocarbonate in the simulation box during 24.4% of the total simulation time. From this we can estimate a free energy of formation of $\Delta A = RT\ln((1-p_{pyro})/p_{pyro}) = 16.8 \pm 1.4$ kJ mol^{-1} ($RT = 14.7$ kJ mol^{-1} at $T = 1{,}773$ K). The minimal/maximal intervals for the continual presence of CO_2 or pyrocarbonate are 0.024 ps/4.84 ps and 0.016 ps/1.52 ps, respectively. By analysing the histograms of the durations of CO_2 or pyrocarbonate intervals (Supplementary Fig. 1), we estimate a CO_2 average lifetime of $\tau_{CO_2} = 0.88$ ps and a pyrocarbonate average life time of $\tau_{pyro} = 0.28$ ps.

The snapshots presented in Fig. 2a–c show, respectively, the approach of CO_3^{2-} to CO_2, the formed pyrocarbonate, and its dissociation to CO_3^{2-} and CO_2. As we can see in Fig. 2d, the identity of the C atoms belonging to the CO_2 or pyrocarbonate varies along the simulation trajectory. We thus looked at all the pyrocarbonate formation/dissociation events and kept track of the C atom part of the CO_2 molecule before the formation of pyrocarbonate and after its dissociation. We found that 72.2% of the time the same C is part of CO_2 before and after a pyrocarbonate ion time interval. Conversely, this means that 27.8% of the time a different C atom is part of the CO_2 after dissociation of the pyrocarbonate.

To go further, we measured the correlation between events in which the C remained the same and between events in which the C changed. Given an event where the C remained the same before the formation and after the dissociation of pyrocarbonate, we measured the frequency of occurrence of n (after the first) consecutive events of the same kind. We also did the same for events where the C had instead changed before the formation and after the dissociation of pyrocarbonate. The results are shown in Fig. 2e, which also plots the theoretical curves $\gamma(1-\gamma)^n$ for 'stay' events and $(1-\gamma)\gamma^n$ for 'change' events, with $\gamma = p_{stay\to change} = p_{stay}(0)$, which assumes no correlation between successive events. The probability of n consecutive 'stay' events is a slowly decaying function of n. Conversely, the probability of consecutive 'change' events decays very rapidly, with a small probability of another change in C after the first one and a very small probability of having two changes after the first one. The cascading of C transfers, through a rapid succession of jump events (as in Fig. 1b), therefore appears unlikely. Hence, in the carbonate melt, the transport of CO_2 (free or bound in pyrocarbonate form) occurs via independent events of formation/dissociation of the pyrocarbonate molecule. This is similar to the Grotthuss mechanism in water, which involves the Zundel cation, $H_3O^+ + H_2O \rightleftharpoons H_5O_2^+$, with oxygen playing the role of the proton. By a random walk model, we estimate the diffusion coefficient of CO_2 to be $D_{Grotthuss} = 8.3 \times 10^{-9}$ m^2 s^{-1}, that is, 2.8 times faster than molecular diffusion of CO_2 (see Supplementary Information for details). It would be of interest in future work to verify, in the presence of an external electric field, whether a cascade of C transfer is likely to occur, similar to the correlated H transfers that have been observed in water under intense electric fields[19].

Pyrocarbonate geometry. Having observed that the pyrocarbonate ion exists in a significant portion of our simulation run, we then proceeded to characterize its geometry by measuring distances and angles, as shown in Fig. 3. Figure 3a plots the distribution of C–C, C–O and C–O* distances. The C–O distribution is quite narrow, peaking at ~1.26 Å, while the C–C and C–O* distance distributions are quite wide. The latter has an asymmetric shape, which is related to the criterion chosen to define the pyrocarbonate molecule (see Methods for more details). Figure 3b shows the normalized distributions of the C–O*–C, O–C–O and O–C–O* angles for pyrocarbonate. The O–C–O and O–C–O* distributions are narrower, while the C–O*–C has a larger dispersion. This suggests that the central C–O*–C bridge is remarkably flexible. For comparison, we also show the O–C–O angle distribution for CO_3^{2-} molecules, which is narrow and peaks at ~120°. In the inset of Fig. 3b, we also show the logarithm of the normalized distribution of the O–C–O angle of the CO_2 molecule and compare it with the case of CO_2 in the gas phase (see Methods). Note that the fluctuations of the O–C–O angle are significantly enhanced in the condensed phase with respect to the gas phase. In fact, the O–C–O angle can even bend to ~120°. Despite the low polarizability of CO_2, we see here that the interactions with the surrounding medium, in this case composed of doubly charged cations and anions, can influence deeply the geometry of CO_2. In particular, the bending of the O–C–O can be related to its interaction with CO_3^{2-} and formation of the pyrocarbonate. Indeed in pyrocarbonate, we observe a O–C–O angle distribution peaking at ~130°.

Supplementary Table 1 compares the mean values of the distances and angles in the pyrocarbonate molecule found in our study with those obtained in silicate melts[18] and in the gas phase, as studied using MP2 calculations by Peeters and co-authors[12]. The extracted values in the $CaCO_3$ solvent are quite similar to those that have been found in silicate melts. The geometry of the pyrocarbonate ions thus appears to stay approximately constant in

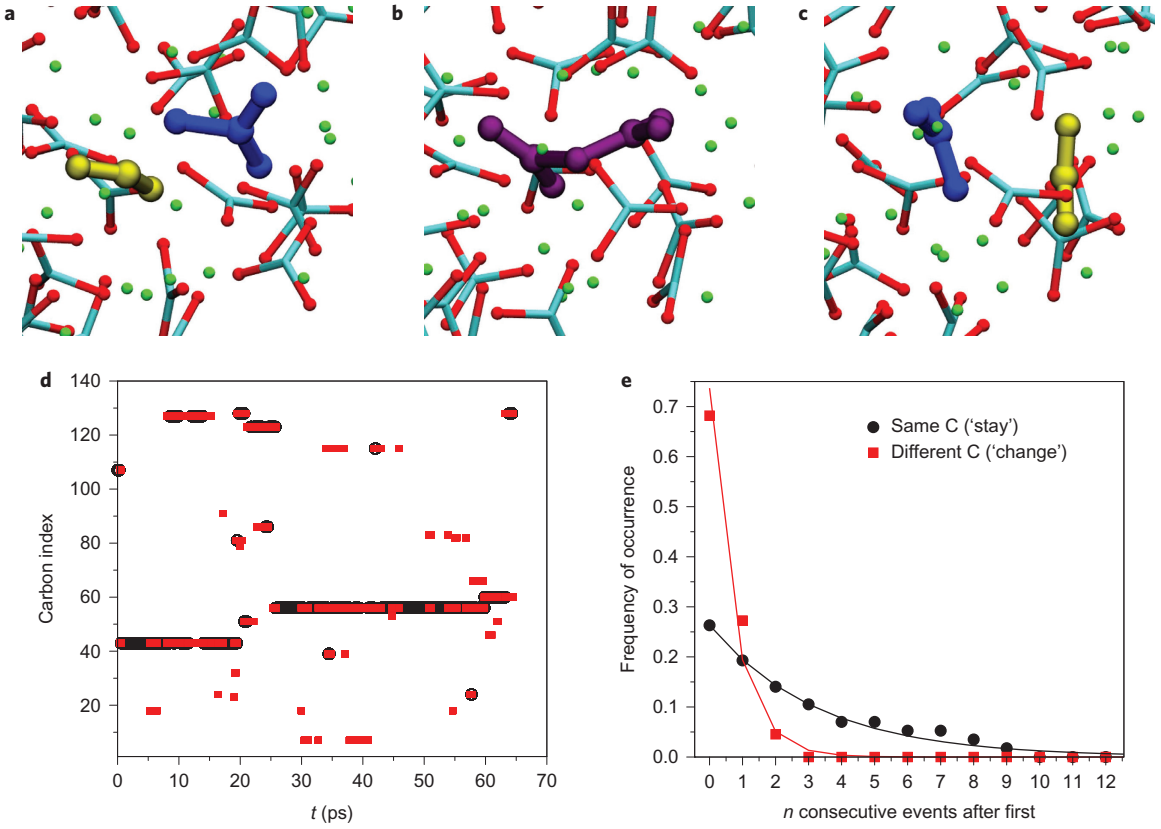

Figure 2 | Formation/dissociation of pyrocarbonate and C transport. a–c, Snapshots representing one instance of the formation/dissociation of pyrocarbonate during the simulation run: CO_2 and CO_3^{2-} approach (**a**), pyrocarbonate $C_2O_5^{2-}$ is formed (**b**) and pyrocarbonate dissociates into CO_3^{2-} and CO_2 (**c**). Carbonate molecules in the solvent are represented by cyan/red sticks, O atoms by red spheres and Ca atoms by green spheres. The CO_2 molecule is shown in yellow, the CO_3^{2-} molecule in blue, and pyrocarbonate in purple. **d**, Indices of the C atoms in CO_2 (black) and pyrocarbonate (red) along the simulation. **e**, The C atom in CO_2 is followed before the formation and after the dissociation of pyrocarbonate. The probability of that C atom staying the same, *n* consecutive times (always reforming the same CO_2 molecule), is shown in black, and the probability of it changing *n* consecutive times (cascading C transfers) is shown in red. The lines are as described in the text.

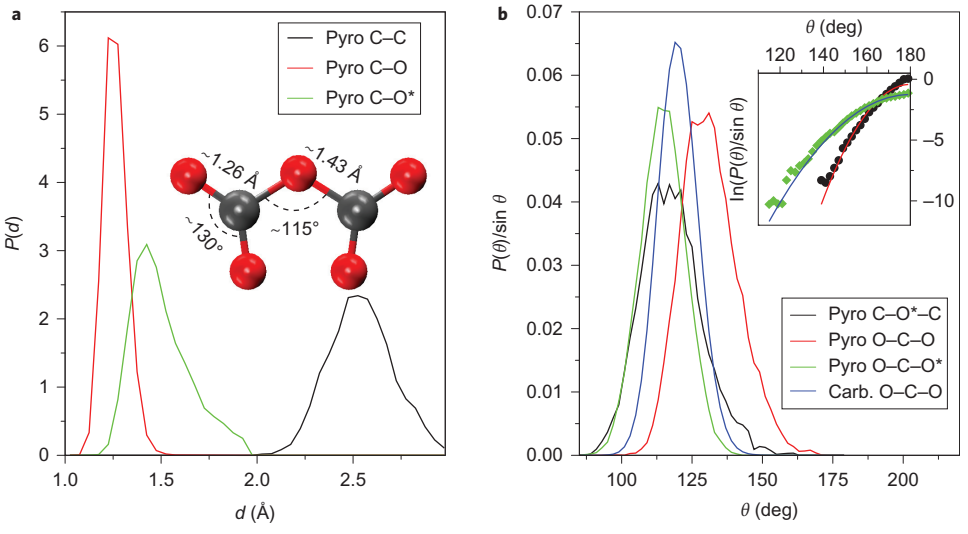

Figure 3 | Geometry of pyrocarbonate anion. a, Distribution of C–C, C–O and C–O* distances measured during the time intervals of existence of $C_2O_5^{2-}$. Inset: average geometry of pyrocarbonate (O, red; C, grey), with values of C–O* and C–O distances and C–O*–C and O–C–O angles shown. **b**, Distribution of C–O*–C, O–C–O and O–C–O* for the pyrocarbonate ion. For comparison, the distribution of the O–C–O angle in CO_3^{2-} is also shown. The distributions are normalized by dividing by sin θ. Inset: natural logarithm of distribution of the O–C–O angle in CO_2 during intervals in which it is present in the $CaCO_3$ melt (green diamonds), and comparison with its behaviour in the gas phase (black circles); see Methods. Parabolic fits of the form $A(\theta - 180°)^2 + B$ are shown as blue and red solid lines for the $CaCO_3$ and gas-phase cases, respectively. Values of the parameters extracted: $A = -0.0025$, $B = -1.25$ ($CaCO_3$) and $A = -0.0059$, $B = -0.42$ (gas).

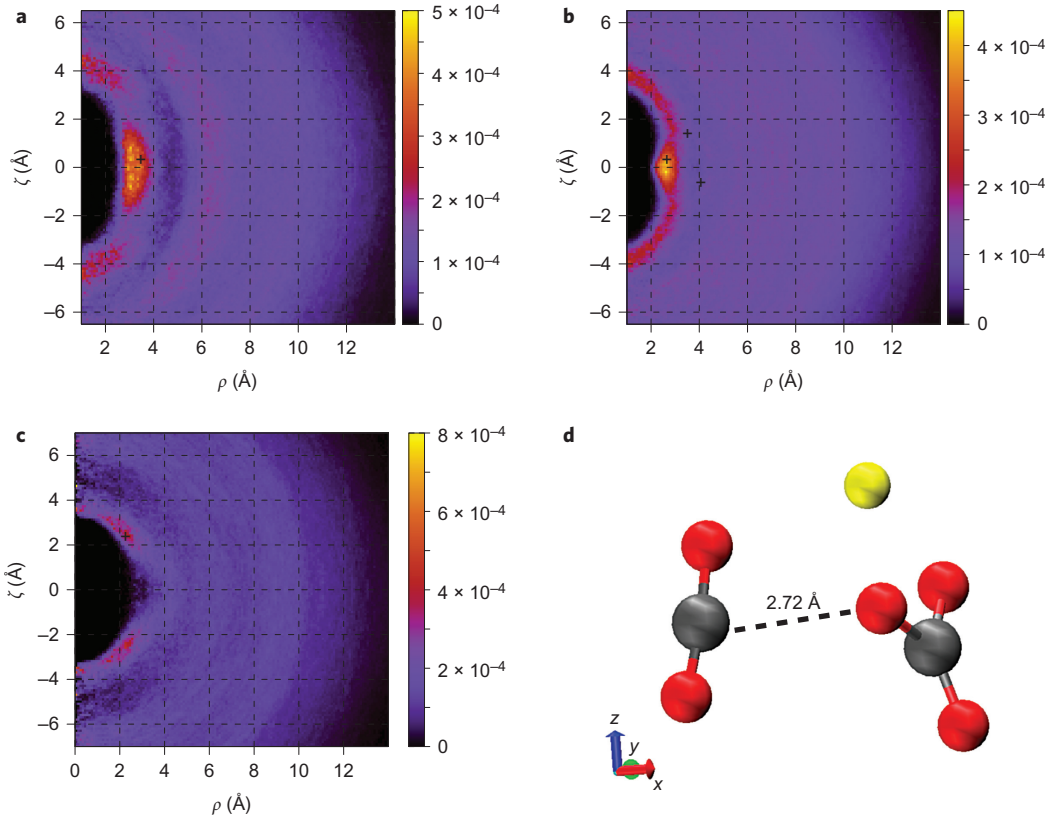

Figure 4 | Solvation structure around the CO_2 molecule. a–c, Two-dimensional colour charts (see Methods) representing the probability of the presence of the following atoms around the CO_2 molecule: C atoms (**a**); O atoms (**b**); and Ca atoms (**c**). The CO_2 molecule is oriented with its O–O axis along the $\hat{\zeta}$ direction, where $\zeta = 0$ is the mid-point of the O–O distance. ζ is thus the projection of an atom position along the O–O axis, and ρ is its distance from the O–O axis. **d**, Gas-phase geometry obtained for a cluster composed of CO_2, CO_3^{2-} and Ca^{2+} (see Methods). Cartesian axes are shown at the bottom. C, grey; O, red; Ca, yellow. Positions of the atoms of carbonate and Ca in the gas phase are marked as + symbols in the respective plots for the condensed phase. Distances are measured in ångstroms.

ionic melts. In contrast, the central C–O*–C angle is much more bent in the condensed phase than in the gas phase, by ~20°. Correspondingly, a smaller C–C distance is found in the condensed phase. We attribute the bending of the pyrocarbonate ion to charge screening occurring in the condensed phase—the charge in the pyrocarbonate ion is mainly carried by the external O atoms, while the central O* is mainly neutral (see, for example, the O–Ca RDFs shown in Supplementary Fig. 2). Charge screening by the surrounding cations therefore allows the charged molecular ends to approach closer to one another than in the gas phase. However, the O–C–O angle and consequently the O–C–O* angle remain quite similar to the gas phase case. To conclude the geometrical analysis of the pyrocarbonate ion, we calculated the O–C–O*–C dihedral angle, shown in Supplementary Fig. 3. We find that the relative orientation in the molecule is rather disordered, probably due to the transients of formation of the pyrocarbonate molecule out of CO_2 and the carbonate ion. However, a preference for periplanar configurations can be observed.

Solvation of molecular CO_2. Not only does CO_2 form $C_2O_5^{2-}$, but even in its molecular state it exhibits specific interactions with CO_3^{2-}. To characterize the solvation structure of molecular CO_2, we built two-dimensional histograms of the structure around the CO_2 molecule (see Methods for details). Figure 4a–c shows these probability density maps for C, O and Ca atoms, respectively. To facilitate the visualization and improve the statistics, we neglected the instantaneous bending of the CO_2 molecule and we built the probability histograms in a cylindrical ρ–ζ coordinate system, where the $\hat{\zeta}$ direction coincides with the O–O unit vector and ρ is the distance from the $\hat{\zeta}$ axis. The zero of the coordinate system was taken at the mid-point of the O–O vector, that is, the average position of the C atom.

Looking at Fig. 4a,b, we note the existence of a preferred position for solvation by CO_3^{2-} in the central area of the ρ–ζ representation. In fact, the largest intensities for the C atoms are observed in the region 2.75 Å $< \rho <$ 3.90 Å and −1.85 Å $< \zeta <$ 1.85 Å. For O atoms, there is instead a bright spot in the area 2.25 Å $< \rho <$ 3.00 Å and −0.55 Å $< \zeta <$ 0.55 Å. Supplementary Fig. 4 presents a histogram of the number of O atoms found in the brightest region evidenced by Fig. 4b. The probability of having at least one O in that region is ~90%. When the central ovoid red area is considered, the probability of having more than three O, and thus more than one carbonate, is close to 80%. This shows that the CO_2 molecule is closely approached by carbonate anions on a preferred pathway, eventually leading to the formation of pyrocarbonate—similar to what has been observed for CO_2 in imidazolium acetates[20]. To obtain a clearer idea of the relative orientation of CO_2 and carbonate in this precursor arrangement, we performed a gas-phase geometry optimization on a cluster composed of CO_2, CO_3^{2-} and Ca^{2+} (see Methods). The resulting geometry is shown in Fig. 4d. We find that one O of the carbonate points directly to the C of CO_2 with a C_{CO_2}–$O_{carb.}$–$C_{carb.}$ angle of ~108°. The distances found in the gas phase are compatible with the two-dimensional colour chart of Fig. 4b, although in the condensed phase the C_{CO_2}–$O_{carb.}$–$C_{carb.}$ angle is closer to ~90°. In addition to this structural analysis, Supplementary Fig. 5 presents a view of the electronic state of the molecules during the formation of the pyrocarbonate, by looking at the centres of the maximally localized Wannier functions.

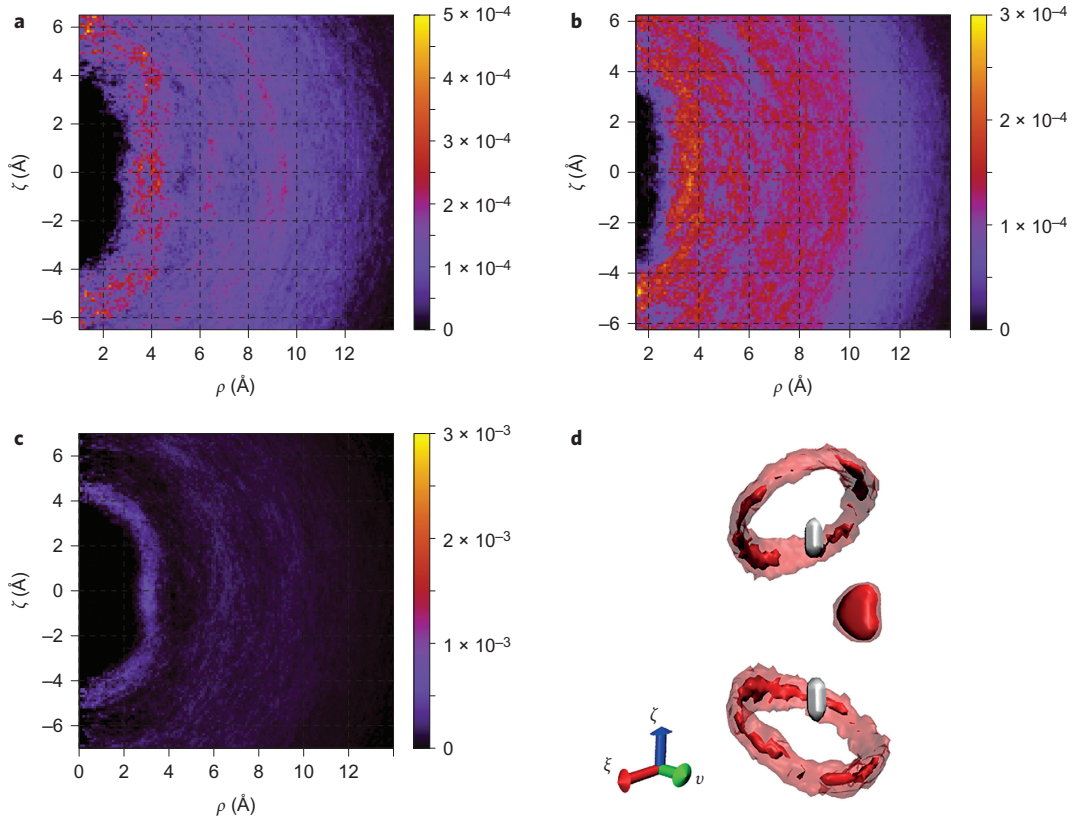

Figure 5 | Solvation structure around the pyrocarbonate ion. a–c, Two-dimensional colour charts (see Methods) representing the probability of the presence of the following atoms around the pyrocarbonate molecule: C atoms (**a**); O atoms (**b**); and Ca atoms (**c**). The $C_2O_5^{2-}$ molecule is oriented with its C–C axis along the $\hat{\zeta}$ direction, where $\zeta = 0$ is the mid-point of the C–C vector. ζ is thus the projection of an atom position along the C–C axis, and ρ is its distance from the C–C axis. The former C of the CO_2 molecule is always placed in the negative ζ portion of the plots. **d**, Three-dimensional density maps of the pyrocarbonate molecule (see Methods). The $\hat{\zeta}$ direction coincides with the C–C axis, the $\hat{\upsilon}$ direction is the perpendicular to $\hat{\zeta}$ passing by O* and $\hat{\xi} = \hat{\upsilon} \times \hat{\zeta}$. Iso-probability surfaces are plotted corresponding to $P = 0.005$ for C (grey), $P = 0.002$ for O (transparent red) and $P = 0.007$ for O (solid red). Distances are measured in ångstroms.

In Fig. 4d, a large excluded volume region is present for Ca atoms around the CO_2 molecule. Interestingly, in the region corresponding to the brightest spot for C and O, a dark spot is visible for Ca. However, Ca does seem to play a role in the approach of carbonate to CO_2. In fact, the position of Ca found in the gas phase (Fig. 4d) corresponds to the intense region just outside the excluded volume. Small bright spots are also visible at $\rho \simeq 0$ and at distances (along $\hat{\zeta}$) three to four times the C–O distance (~1.17 Å), where carbonate ions are already interposed to screen the Ca^{2+} charge.

Pyrocarbonate solvation. In contrast to the case of molecular CO_2, the solvation structure of pyrocarbonate is more diffuse. Given the mostly periplanar symmetry indicated by the dihedral angle (Supplementary Fig. 3), we continue to neglect one dimension and produce two-dimensional histograms, analogous to what is shown in Fig. 4 for the CO_2 molecule. In this case, the vertical $\hat{\zeta}$ axis coincides with the C–C direction, and ρ is the distance from this axis. The centre of the coordinate system is taken at the mid-point of the C–C vector (see Methods). We also keep track of the C atom that is part of the CO_2 molecule before the formation of the pyrocarbonate, and the charts are constructed in such a way that the C formerly belonging to CO_2 is always found at the bottom of the plots.

Figure 5a presents two-dimensional histograms for the C atoms around the pyrocarbonate. The solvation of pyrocarbonate by C atoms is almost uniform, with a small dent in the central region around $\zeta \simeq 0$ and $\rho \simeq 3$ corresponding to a modest electrostatic attraction by the central O* atom of pyrocarbonate and repulsion by the two C atoms. In addition, we observe three consecutive solvation shells, with the first being the most intense. Figure 5b shows the equivalent two-dimensional histogram for O atoms. Given that O is attached to C in carbonate ion units, the positions of the O atoms follows from that of the C, although we see here that the situation for the O appears much more diffuse, corresponding to a random orientation of the plane of the carbonate molecules in the liquid phase. One small bright spot is visible at $\zeta \simeq -4.5$ and $\rho \simeq 0$. Because the C formerly in CO_2 is, by construction, always found in the negative ζ portion, this possibly indicates that another CO_3^{2-} was or is in competition for the formation of pyrocarbonate. This is compatible with Supplementary Fig. 4, where we see that the most intense spots in Fig. 4b correspond to one or two carbonate molecules close to CO_2.

Figure 5c shows the two-dimensional histogram for Ca atoms. As in the case of C atoms, we observe an almost uniform first solvation shell with a central dent, corresponding to attraction by the O* atom and repulsion by the C atoms of pyrocarbonate. Furthermore, we notice a small bright spot at $\rho \simeq 0$, $\zeta \simeq 4.5$, probably corresponding to the fact that Ca is close to the previous CO_3^{2-} unit, rather than to the previous CO_2. Finally, Fig. 5d plots the three-dimensional isoprobability surfaces for the atoms composing the pyrocarbonate, derived from three-dimensional histograms calculated as described in the Methods. The plot shows how the position of the O in pyrocarbonate is orientationally disordered in the condensed phase, probably due to the transients of formation/dissociation. When the isoprobability value is increased, distinct spots appear that are consistent with periplanar configurations, $0° < \varphi < 30°$ or $150° < \varphi < 180°$, and with configurations with the two pairs of external O nearly perpendicular to each other, $80° < \varphi < 110°$ (Supplementary Fig. 3).

Conclusions

In summary, our study of CO_2 solvation in molten calcium carbonate by FPMD confirms the presence of the pyrocarbonate anion and of the equilibrium $CO_2 + CO_3^{2-} \rightleftharpoons C_2O_5^{2-} \rightleftharpoons CO_3^{2-} + CO_2$. We have observed how the transport of CO_2 in molten carbonate occurs in a manner similar to the Grotthuss mechanism in water, and we term this the 'oxo-Grotthuss mechanism'. We have characterized the geometry of pyrocarbonate and found it has a periplanar configuration, with the central C–O*–C bridge much more bent than in the gas phase, due to charge screening by the counterions. Furthermore, we have observed that the interaction between CO_2 and CO_3^{2-} leading to the formation of pyrocarbonate occurs along a preferred pathway, with the carbonate ion approaching CO_2 'laterally'. The enhanced transport of CO_2 by O^{2-} exchange—three times faster than molecular diffusion—may also explain the diffusivity of CO_2 in mixed oxide–carbonate materials[15].

The CO_2/CO_3^{2-} equilibrium can also be described in the framework of oxo-acidity, with CO_2 being the acid and CO_3^{2-} its conjugated base. In this context, Grotthuss-like transport may be rather general when an acid is dissolved in its conjugated base.

Methods

FPMD simulations. We have studied a system originally composed of 127 CO_3^{2-} carbonate anions, 127 Ca^{2+} calcium cations and one CO_2 molecule (638 atoms, 4,080 valence electrons). We fixed the side of the cubic simulation box to be $L = 20.054$ Å, which gives a density of $\rho = 2.63$ g cm^{-3}. The CO_2 concentration is thus 0.206 mol l^{-1}, a value typical for alkali molten salts under 1 atm of CO_2[21]. We set the temperature, controlled by the Nosé–Hoover thermostat chain[22,23] with a time constant $\tau = 0.5$ ps, at $T = 1{,}773$ K. This thermodynamic point is located, according to the pure $CaCO_3$ melting curve obtained by Suito *et al.*[24] and Spivak *et al.*[25], along the melting curve of disordered pure calcite (no CO_2).

We performed FPMD simulations based on DFT and the Born–Oppenheimer dynamics, and used the software CP2K (ref. 26) and in particular the Quickstep algorithm[27]. The latter employs a hybrid Gaussian plane-wave method (GPW)[28]. The Goedecker–Teter–Hutter (GTH) norm-conserving pseudo-potentials[29–31] were used to replace the core electrons. We cut off the electronic density at 400 Ry and used NN50 smoothing to apply the exchange–correlation potential. For C and O atoms, a triple-zeta valence doubly polarized (TZV2P) basis set was used[32], and for Ca atoms we used a double-zeta valence plus polarization (DZVP) basis set optimized for molecules[33]. The exchange–correlation interactions were taken into account by the gradient-corrected BLYP functional[34,35]. Dispersive interactions corrections were added by using the DFT-D2 scheme[36], with a cutoff of 40 Å.

The starting configuration was taken from previous equilibrated FPMD simulations of pure liquid $CaCO_3$ (128 units)[17] after having replaced one CO_3^{2-} with CO_2 and having erased one Ca^{2+} from the simulation box. We ran the simulation in the canonical *NVT* ensemble, with the simulation time step set to 0.5 fs and periodic boundary conditions. The trajectory at every time step was stored for post–run–time analysis. We accumulated the trajectory for ~65 ps (130,000 simulation steps).

In addition, we also performed a FPMD simulation of CO_2 in the gas phase, as well as geometry optimizations of the pyrocarbonate ion in the gas phase and a cluster composed of CO_2, CO_3^{2-} and Ca^{2+} (shown in Fig. 4d). Details for these can be found in Supplementary Section 'Methods'.

Analysis. Analysis of the simulation trajectory was performed using an in-house analysis suite. To define molecules from the atomic positions at each time step, we used a depth first search (DFS) closure algorithm[37]. A particular 'hysteresis' criterion was applied to define whether, in a given time frame, there was molecular CO_2 or a pyrocarbonate ion. If molecular CO_2 was in the previous time frame, we accounted for the formation of the pyrocarbonate in the current frame only when the C–O* distance was less than 1.7 Å. On the other hand, if we had pyrocarbonate in the previous frame, we accounted for a dissociation event in the current frame only when the C–O* distance became larger than 1.95 Å. This criterion allowed smoothing of the behaviour observed when a simple distance cutoff criterion is used, and was inspired by the criteria used for correlations in hydrogen bond dynamics in water[38].

To build the two-dimensional colour charts around the CO_2 molecules (Fig. 4), the coordinates were first recentred, with the centre $\mathbf{r}_c$ defined as the mid-point of the CO_2 O–O vector. We defined the $\hat{\zeta}$ direction as the O–O unit vector, and then calculated the coordinate ζ of a given atom as $\zeta = \mathbf{r}'_i \cdot \hat{\boldsymbol{\zeta}}$, where $\mathbf{r}'_i = \mathbf{r}_i - \mathbf{r}_c$. Coordinate ρ is given by $\rho = \sqrt{||\mathbf{r}'_i||^2 - \zeta^2}$ or equivalently by $\rho = ||\mathbf{r}'_i - \zeta\hat{\boldsymbol{\zeta}}||$. We binned the space by $\Delta\zeta = \Delta\rho = 0.1$ Å in the intervals between $-L/2$ and $L/2$ for ζ and 0 and $\sqrt{2}L/2$ for ρ. The two-dimensional intensity histogram was normalized by dividing by the product of the number of steps, by the number of particles of type α (α = C, O, Ca) and by the bin volume $2\pi\rho\Delta\rho\Delta\zeta$.

For construction of the two-dimensional colour charts around the pyrocarbonate ion (Fig. 5), we followed an analogous procedure, with the only difference being that the C–C direction was now taken as $\hat{\zeta}$ and the mid-point of the C–C vector as centre. Furthermore, we specifically took the beginning of the C–C vector corresponding to the C atom that was part of the CO_2 molecule just before the formation of the pyrocarbanate ion. The former C of the CO_2 molecule was thus always found in the negative ζ portion of the plots.

We also built three dimensional density maps for C and O (for example, Fig. 5d). In those plots, axis $\hat{\zeta}$ coincides with the C–C direction, the $\hat{v}$ axis is obtained from CO*–(CO*·$\hat{\zeta}$)$\hat{\zeta}$ and $\hat{\xi} = \hat{v} \times \hat{\zeta}$. We recentred the coordinates around the mid-point of the C–C vector $\mathbf{r}_c$, $\mathbf{r}'_i = \mathbf{r}_i - \mathbf{r}_c$. The new coordinates were thus $\xi = \mathbf{r}'_i \cdot \hat{\boldsymbol{\xi}}$, $v = \mathbf{r}'_i \cdot \hat{\boldsymbol{v}}$ and $\zeta = \mathbf{r}'_i \cdot \hat{\boldsymbol{\zeta}}$. We binned the space by $\Delta\xi = \Delta v = \Delta\zeta = 0.1$ Å between –6.0 and 6.0 Å. The intensity histograms were normalized by dividing by the number of steps, the number of particles of type α (α = C, O, Ca) and by the volume of the bin $\Delta\xi\Delta v\Delta\zeta$. Molecular representations and iso-probability surfaces were visualized using the software VMD[39].

Received 26 July 2015; accepted 7 January 2016; published online 29 February 2016

References

1. Gaillard, F., Malki, M., Iacono-Marziano, G., Pichavant, M. & Scaillet, B. Carbonatite melts and electrical conductivity in the asthenosphere. *Science* **322,** 1363–1365 (2008).
2. Jones, A. P., Genge, M. & Carmody, L. Carbonate melts and carbonatites. *Rev. Mineral. Geochem.* **75,** 289–322 (2013).
3. Kaminsky, F., Wirth, R., Schreiber, A. & Thomas, R. Nyerereite and nahcolite inclusions in diamond: evidence for lower-mantle carbonatitic melts. *Mineral. Mag.* **73,** 797–816 (2009).
4. Stoppa, F., Jones, A. P. & Sharygin, V. Nyerereite from carbonatite rocks at Vulture volcano: implications for mantle metasomatism and petrogenesis of alkali carbonate melts. *Cent. Euro. J. Geosci.* **1,** 131–151 (2009).
5. Kaminsky, F. Mineralogy of the lower mantle: a review of 'super-deep' mineral inclusions in diamond. *Earth Sci. Rev.* **110,** 127–147 (2012).
6. Dasgupta, R. & Hirschmann, M. M. The deep carbon cycle and melting in Earth's interior. *Earth Planet. Sci. Lett.* **298,** 1–13 (2010).
7. Dasgupta, R. & Hirschmann, M. M. Melting in Earth's deep upper mantle caused by carbon dioxide. *Nature* **440,** 659–662 (2006).
8. Chery, D., Lair, V. & Cassir, M. CO_2 electrochemical reduction into CO or C in molten carbonates: a thermodynamic point of view. *Electrochim. Acta* **160,** 74–81 (2015).
9. Chery, D., Albin, V., Lair, V. & Cassir, M. Thermodynamic and experimental approach of electrochemical reduction of CO_2 in molten carbonates. *Int. J. Hydrogen Energy* **39,** 12330–12339 (2014).
10. Kanai, Y., Fukunaga, K., Terasaka, K. & Fujioka, S. Mass transfer in molten salt and suspended molten salt in bubble column. *Chem. Eng. Sci.* **100,** 153–159 (2013).
11. Claes, P., Moyaux, D. & Peeters, D. Solubility and solvation of carbon dioxide in the molten $Li_2CO_3/Na_2CO_3/K_2CO_3$ (43.5:31.5:25.0 mol-%) eutectic mixture at 973K. I. Experimental part. *Eur. J. Inorg. Chem.* **1999,** 583–588 (1999).
12. Peeters, D., Moyaux, D. & Claes, P. Solubility and solvation of carbon dioxide in the molten $Li_2CO_3/Na_2CO_3/K_2CO_3$ (43.5:31.5:25.0 mol-%) eutectic mixture at 973K. II. Theoretical part. *Eur. J. Inorg. Chem.* **1999,** 589–592 (1999).
13. Burna, P. J., Grein, F. & Passmore, J. Density functional theory (DFT) calculations on the structures and stabilities of $[C_nO_{2n+1}]^{2-}$ and $[C_nO_{2n+1}]X_2$ polycarbonates containing chainlike $(CO_2)_n$ units (n=2–6; X=H or Li). *Can. J. Chem.* **89,** 671–687 (2011).
14. Frapper, G. & Saillard, J.-Y. Search for new allotropic forms of carbon dioxide and carbon disulfide: a density functional study of CX_2-based oligomers (X= O, S). *J. Am. Chem. Soc.* **122,** 5367–5370 (2000).
15. Zhang, L. *et al.* First spectroscopic identification of pyrocarbonate for high CO_2 flux membranes containing highly interconnected three dimensional ionic channels. *Phys. Chem. Chem. Phys.* **15,** 13147–13152 (2013).
16. Zeller, K.-P., Schuler, P. & Haiss, P. The hidden equilibrium in aqueous sodium carbonate solutions—evidence for the formation of the dicarbonate anion. *Eur. J. Inorg. Chem.* 168–172 (2005).
17. Vuilleumier, R., Seitsonen, A., Sator, N. & Guillot, B. Structure, equation of state and transport properties of molten calcium carbonate ($CaCO_3$) by atomistic simulations. *Geochim. Cosmochim. Acta.* **141,** 547–566 (2014).
18. Vuilleumier, R., Seitsonen, A. P., Sator, N. & Guillot, B. Carbon dioxide in silicate melts at upper mantle conditions: insights from atomistic simulations. *Chem. Geol.* **418,** 77–88 (2015).
19. Saitta, A. M., Saija, F. & Giaquinta, P. V. *Ab initio* molecular dynamics study of dissociation of water under an electric field. *Phys. Rev. Lett.* **108,** 207801 (2012).
20. Kelemen, Z. *et al.* An abnormal N-heterocyclic carbene–carbon dioxide adduct from imidazolium acetate ionic liquids: the importance of basicity. *Chem. Eur. J.* **20,** 13002–13008 (2014).
21. Chery, D., Lair, V. & Cassir, M. Overview on CO_2 valorization: challenge of molten carbonates. *Front. Energy Res.* **3,** 43 (2015).
22. Nosé, S. A molecular-dynamics method for simulations in the canonical ensemble. *Mol. Phys.* **52,** 255–268 (1984).

23. Nosé, S. A unified formulation of the constant temperature molecular-dynamics methods. *J. Chem. Phys.* **81,** 511–519 (1984).
24. Suito, K. *et al.* Phase relations of $CaCO_3$ at high pressure and high temperature. *Am. Mineral.* **86,** 997–1002 (2001).
25. Spivak, A. V., Litvin, Y. A., Ovsyannikov, S. V., Dubrovinskaia, N. A. & Dubrovinsky, L. S. Stability and breakdown of $Ca^{13}CO_3$ melt associated with formation of ^{13}C-diamond in static high pressure experiments up to 43 GPa and 3900 K. *Solid State Chem.* **191,** 102–106 (2012).
26. Hutter, J., Iannuzzi, M., Schiffmann, F. & VandeVondele, J. CP2K: atomistic simulations of condensed matter systems. *WIREs Comput. Mol. Sci.* **4,** 15–25 (2014).
27. VandeVondele, J. *et al.* QUICKSTEP: fast and accurate density functional calculations using a mixed Gaussian and plane waves. *Comp. Phys. Commun.* **167,** 103–128 (2005).
28. Lippert, G., Hutter, J. & Parrinello, M. A hybrid Gaussian and plane wave density functional scheme. *Mol. Phys.* **92,** 477–487 (1997).
29. Goedecker, S., Teter, M. & Hutter, J. Separable dual-space Gaussian pseudopotentials. *Phys. Rev. B* **54,** 1703–1710 (1996).
30. Hartwigsen, C., Goedecker, S. & Hutter, J. Relativistic separable dual-space Gaussian pseudopotentials from H to Rn. *Phys. Rev. B* **58,** 3641–3662 (1998).
31. Krack, M. Pseudopotentials for H to Kr optimized for gradient-corrected exchange-correlation functionals. *Theor. Chem. Acc.* **114,** 145–152 (2005).
32. VandeVondele, J. *et al.* The influence of temperature and density functional models in *ab initio* molecular dynamics simulation of liquid water. *J. Chem. Phys.* **122,** 014515 (2005).
33. VandeVondele, J. & Hutter, J. Gaussian basis sets for accurate calculations on molecular systems in gas and condensed phases. *J. Chem. Phys.* **127,** 114105 (2007).
34. Becke, A. D. Density-functional exchange-energy approximation with correct asymptotic behavior. *Phys. Rev. A* **38,** 3098–3100 (1988).
35. Lee, C., Yang, W. & Parr, R. G. Development of the Colle–Salvetti correlation energy formula into a functional of the electron density. *Phys. Rev. B* **37,** 785–789 (1988).
36. Grimme, S. Semiempirical GGA-type density functional constructed with a long-range dispersion correction. *J. Comput. Chem.* **27,** 1787–1799 (2006).
37. Cormen, T. H., Leiserson, C. E., Rivest, R. L. & Stein, C. *Introduction to Algorithms* (MIT Press, 1990).
38. Laage, D. & Hynes, J. T. A molecular jump mechanism of water reorientation. *Science* **311,** 832–835 (2006).
39. Humphrey, W., Dalke, A. & Schulten, K. VMD—visual molecular dynamics. *J. Mol. Graph.* **14,** 33–38 (1996).

Acknowledgements

The authors thank M. Cassir, V. Lair, B. Guillot, F. Gaillard, V. Haigis and A. Boutin for discussions. The research reported herein was funded by PSL Research University (project COOCAR, grant ANR-10-IDEX-0001-02) and Agence Nationale de la Recherche (project ELECTROLITH, grant ANR-2010-BLAN-621-03). This work was performed using HPC resources from GENCI (grants 2013-082309, 2014-082309 and 2015-082309) and IDRIS (grant 'Grand Challenge' 100577). The authors acknowledge PRACE for awarding access to Resource Curie, based in France at CEA Bruyères-le-Chatel (preparatory access allocation 2010PA2746).

Author contributions

R.V. performed the FPMD simulations. D.C. analysed the trajectories, prepared the figures and wrote the manuscript. All authors designed the research, discussed the results and revised the manuscript.

Additional information

Supplementary information is available in the online version of the paper. Reprints and permissions information is available online at www.nature.com/reprints. Correspondence and requests for materials should be addressed to F.X.C. and R.V.

Competing financial interests

The authors declare no competing financial interests.